

Eksploatacja i Niezawodnosc - Maintenance and Reliability

Volume 29 (2027), Issue 3

https://ein.org.pl

The Polish Maintenance Society

A study of the static and fatigue testing of composite profiles with notches

Patryk Różyło[1,*], Jakub Paśnik[1], Adam Stawiarski[2], Małgorzata Chwał[2], Paweł Romanowicz[2], Marek Barski[2], Hubert Dębski[1]

[1] Politechnika Lubelska, Poland
[2] Politechnika Krakowska, Poland
* Corresponding Author: p.rozylo@pollub.pl

Received: 11 June 2026
Revised: 5 October 2026
Accepted: 30 October 2026
Online: 19 November 2026

This is an open access article under the CC BY 4.0 license

Abstract

The study applied and compared several non-destructive testing methods to evaluate fatigue damage in thin-walled composite profiles with notches. The static and fatigue tests were performed on carbon-epoxy composite specimens with a lay-up of $[45/-45/45/-45]_s$. As part of the experimental testing, static tensile tests were performed to determine the limit loads of the composite profiles. Based on the preliminary static tensile tests, the fatigue test parameters were estimated, and the tests were carried out using a fatigue testing machine and several non-destructive testing methods. We carried out an experimental damage assessment using the following additional non-destructive testing methods: passive thermography, acoustic emission, and digital microscopy. Preliminary signs of damage were identified, and the fatigue response of composite structures was determined during low-cycle fatigue testing. The study assessed fatigue damage using both quantitative and qualitative methods, particularly in the context of the research conducted.

Keywords: *static strength tests, low-cycle fatigue tests, non-destructive testing methods, damage initiation, composite specimens with notches*

Article citation:
Różyło P, Paśnik J, Stawiarski A, Chwał M, Romanowicz P, Barski M, Dębski H, A study of the static and fatigue testing of composite profiles with notches, Eksploatacja i Niezawodnosc – Maintenance and Reliability 2027: 29(3) http://doi.org/10.17531/ein/242348

Highlights

- NDT methods were used to assess the damage to composite.
- The fatigue response of composite structures was determined during low-cycle fatigue testing.
- Preliminary signs of damage were identified.

1. Introduction

Fatigue is a key aspect of materials engineering, directly affecting the reliability and durability of engineering structures. Under cyclic loading, damage in the material gradually increases and spreads, reducing load-bearing capacity and ultimately causing a complete loss of structural integrity. This can occur even when the applied stress is below the yield strength. Standard fatigue testing of metals has been conducted since the beginning of the 20th century [1,2]. This has led to the development of advanced mathematical and experimental models that describe crack formation and propagation in homogeneous materials. In recent years, fatigue testing of composite materials has advanced rapidly, especially for polymer matrix composites [3–6]. With advances in materials engineering, simulation capabilities, and computing resources, fiber composites have surged in popularity and use in materials research. Currently, these materials are among the most widely used structural materials in the aviation and aerospace industries, the automotive industry, wind energy, and the military industry [3]. Their properties, which are unheard of in conventional materials, mainly the favorable strength-to-weight ratio and the ability to design and determine specific mechanical properties, allow for a wide range of applications for these materials. This, in turn, enables a significant reduction in structural weight while maintaining high tensile and fatigue strength. Despite widespread interest, the fatigue strength of fiber-reinforced polymer composites remains a complex and insufficiently investigated problem. In view of this, the issue requires an interdisciplinary approach spanning many fields of science, including mechanics, materials science, and non-destructive testing methods [5], to name a few. However, the

continuous development of composite materials, especially polymer-based composites reinforced with carbon fibers, has forced a revision of the classic approach to fatigue strength testing. Due to their specific structure, which includes long fibers arranged in a specific direction and bonded with a matrix, these composites are characterized by strong anisotropy of mechanical properties, complex internal architecture, and non-uniform stress distribution, which makes their response to cyclic loading much more complicated than in the case of homogeneous materials [3–5,7,8] The work of Harris [3] and Talreja and Singh [4] indicates that the high strength-to-weight ratio and the possibility of designing mechanical properties make CFRP an extremely attractive material, but at the same time susceptible to complex fatigue degradation mechanisms, which have not yet been sufficiently studied. Reifsnider and Case [5] proposed the concept of damage tolerance, emphasizing the need to account for the progressive degradation of properties throughout the life cycle of a composite structure. Unlike metals, where the dominant fatigue mechanism is the initiation and propagation of a single crack, carbon fiber reinforced polymer (CFRP) laminates exhibit multiple local degradation processes. These include matrix microcracks, fiber-matrix interfacial delamination, interlaminar delamination, and fiber breakage, which can occur simultaneously and interact [6–11]. Experimental studies show that multiple matrix microcracks often initiate degradation, leading to local stiffness loss and contributing to delamination initiation, which in turn causes stress concentrations in adjacent laminate layers [6,8]. Liu et al. [6] characterized in detail the progressive nature of damage in CFRP laminates, while Samborski [11] analyzed the influence of mechanical couplings on the delamination process using numerical analysis of the DCB test configuration. Geometric factors and manufacturing imperfections, such as notches, holes, air bubbles, or local fiber-orientation disturbances, also significantly affect the fatigue life of composites. Wang et al. [9] and Romanowicz and Muc [12] studied these issues and showed that local stress concentrations significantly accelerate damage initiation. In their work, Muc et al. [13] proposed a model of progressive degradation in notched multilayer structures, combining experiments with finite element method simulations, which enabled a quantitative assessment of the influence of geometry on fatigue life. In the publication [14] the authors presented the capabilities of various non-destructive techniques for the characterization of CFRP notched specimens in fatigue testing. The authors performed quasi-static and fatigue tests, monitoring the material's stress state using digital image correlation (DIC). The results show that validating DIC and vibration response can be a useful tool for monitoring fatigue damage development and estimating damage scale in composite materials. Fatigue models for CFRP composites span a wide range of approaches, from empirical models [10,15] through energy and micromechanical methods [16–18] to advanced continuum damage mechanics models implemented in FEM environments [17,19–21]. Quaresimin, Susmel, and Talreja [16] is a key reference for assessing laminate durability under multiaxial loads. These models have been developed for the analysis of progressive degradation of material properties, which enables the simulation of the entire fatigue process, from damage initiation to complete failure. The work of Hofman et al. [17] and Khan et al. [22] presents modern approaches to modeling interlaminar delamination that account for local stress coefficients and the effects of cyclic loading. Studies on notched specimens mainly focus on static testing. The authors of the paper [23] conducted experimental and analytical research on Single-Edge Notched Tension (SENT) specimens in tensile tests. They carried out the tests at various temperatures and used non-destructive techniques to observe damage progression. The study also tested notched specimens [24]. The virtual wave concept method was used to observe damage progression beneath the specimen’s surface. Both this study and the following studies used closed-notch specimens (with a hole in the center of the specimen) [25,26].

Non-destructive testing techniques are an important complementary method to fatigue testing, enabling real-time monitoring of damage evolution and validation of numerical models. Acoustic emission [27–29] allows the identification of dominant degradation mechanisms based on signal characteristics. This method enables analysis of a variety of signals that provide information on the timing of defect initiation during specimen loading, as well as the type of defect. These signals may include: absolute energy, duration, frequency [30], number of hits and counts, amongst others. Infrared thermography [31–33] enables the observation of local effects of energy dissipation and self-heating, which significantly

accelerate the fatigue process. Katunin [31,32] showed that thermal effects should be treated as an integral part of composite fatigue description. Another technique for diagnosing composite damage is digital image correlation [34], which provides information on deformation locations and stress concentrations, while computed tomography [35,36] enables three-dimensional analysis of internal damage development. Wang et al. [35] offer an advanced, interdisciplinary approach that combines in situ X-ray tomography, DVC analysis, and machine learning methods, opening new perspectives for composite fatigue modeling. The literature also frequently reports new non-destructive techniques for assessing the condition of composite materials. Although eddy current testing is a well-known method used mostly for non-destructive testing of electrically conductive materials, studies such as [37], which use this effect to test composites, are beginning to appear. Changes in electrical conductivity and permittivity, measured during testing with this technique, provide an evaluation of composite manufacturing quality by identifying local defects, such as polymer degradation or thermal impacts.

In fatigue analyses of fiber composites, numerical methods based on finite element analysis are increasingly used, allowing quantitative modeling of progressive material degradation while accounting for microdamage mechanisms and couplings between different degradation mechanisms. The integration of FEM models with the results of Non-Destructive Testing (NDT) methods (IRT, DIC, AE, CT) is particularly promising from the point of view of validation and calibration of simulations: the combination of in situ tomographic data with the analysis of deformation fields during fatigue allows for direct validation of numerical damage predictions and has been successfully presented in the research of Wang et al. [35]. Such interdisciplinary approaches confirm that advanced, validated finite element analysis-based models are among the most important tools for quantitative fatigue analysis of composites, enabling realistic representation of degradation mechanisms and reliable prediction of CFRP structure durability.

The international literature has also carried out significant research on dynamic studies of composite shell structures. This research has made a significant contribution to expanding further research in this field [38–40]. The following papers present equally important issues relating to composite materials and mechanical phenomena [41,42].

In summary, contemporary fatigue testing of CFRP composites indicates that a comprehensive description of their durability requires integrating experimental testing, non-destructive diagnostic methods, and advanced numerical simulations based on the finite element method. The multi-stage, multi-mechanism nature of degradation makes classical approaches based solely on S-N curves insufficient, and developing validated FEM models that capture actual damage mechanisms is currently one of the most innovative and promising directions in fatigue research on fiber composites. Future publications will use FEM models.

The novelty of the research lies in applying several complementary damage monitoring techniques and, more importantly, using them simultaneously to establish a link between changes observed at different levels of degradation in thin-walled composite profiles. Static analysis determined the effect of the damage process on the structure's mechanical response, while fatigue testing tracked damage evolution as a function of the number of loading cycles. Thermography provided information on local changes in the temperature field associated with degradation, acoustic emission identified active damage mechanisms, and stiffness-decline analysis allowed a quantitative assessment of degradation progression in mechanical properties. These results were cross-checked with microscopic observations to directly identify and interpret damage mechanisms at the microstructural level. This approach provided a more comprehensive picture of damage development than a single diagnostic technique could. Significantly, it is now possible to correlate the signals recorded by the individual methods with specific stages of profile degradation and characteristic damage mechanisms. This not only enables damage detection, but also more accurately determines its nature, stage of advancement, and relationship to changes in the structure's overall stiffness.

2. The subject of the study

The research focused on thin-walled composite structures made of carbon fiber-reinforced polymer (CFRP). The specimens were manufactured using an autoclave technique (external company) and cut to the required size with a water jet. The test specimens had a specific arrangement of composite material

layers (commonly known as composite lay-up) $[45/-45/45/-45]_s$. The geometric parameters of the specimens were determined through preliminary research activities to adequately characterize the structure's behavior during static and dynamic testing. Figure 1 shows a schematic visualization of the test specimens, together with their geometric parameters.

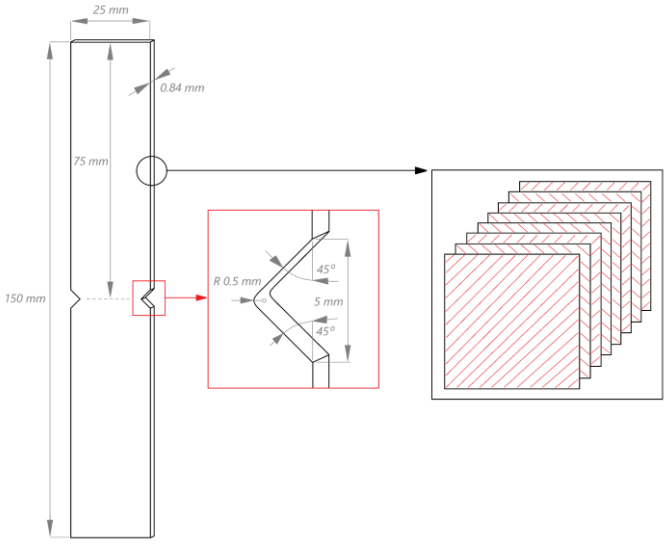


Figure 1. Geometrical parameters and composite lay-up of test specimens.

The specimens intended for experimental testing were prepared with the utmost care. Three specimens were prepared for static testing and three for fatigue testing for experimental testing. All specimens had the same geometric parameters and laminate layer arrangement. The specimens used for the experimental tests were characterized by material properties determined from static tests in accordance with the relevant ISO standards. The material properties (mechanical and strength) were determined based on the aforementioned dedicated standards: PN-EN ISO 527–5 (tensile strength test), PN-EN ISO 14126 – (compression strength test), and PN-EN ISO 14129 (shear strength test). Previous publications present the specified material parameters, while [43] describes in detail the methodology for determining the properties of CFRP composites. The material parameters were determined using electrical resistance strain gauge technology, which enabled the most accurate results possible in the experimental tests. Table 1 provides detailed information on the specified material parameters, showing the composite material's mechanical and strength properties. For this publication, we examined at least five specimens specially prepared to test the material properties for each test type, in accordance with the aforementioned standards. The table below shows the mean values from the material tests, together with the standard deviation for each value.

Table 1. The material properties of the CFRP composite (average values with standard deviation).

Mechanical properties		Strength properties	
Young's modulus E_1 0° (MPa)	143,528.5 (±9,271.6)	Tensile strength F_{TU} 0° (MPa)	2,220.7 (±200.6)
Young's modulus E_2 90° (MPa)	5,826.3 (±108.9)	Tensile strength F_{TU} 90° (MPa)	49 (±4.2)
Poisson's ratio ν_{12}	0.36 (±0.04)	Compression strength F_{CU} 0° (MPa)	641 (±84.6)
Kirchhoff's modulus G_{12} (MPa)	3,845.5 (±332.5)	Compression strength F_{CU} 90° (MPa)	114 (±5.8)
		Shear strength F_{SU} ±45° (MPa)	83.5 (±2.5)

The properties presented in Table 1 are the average results of a series of tests conducted to determine the material's parameters. The correctness of the aforementioned material parameters has been carefully verified. These parameters were presented in an example research paper that was published as part of a previous study [44].

During the initial inspection of the specimens prepared for testing, we estimated that the specimens' preparation quality was satisfactory. The thickness of the analyzed specimens was consistent with the initial assumptions, as confirmed by preliminary analyses using a digital microscope with a depth-of-field option. Figure 2 presents an example visualization showing a selected research specimen (in the context of thickness and structure analysis).

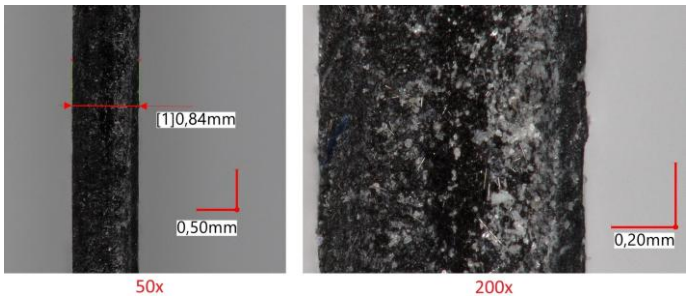


Figure 2. A microscopic assessment of the thickness of composite specimens.

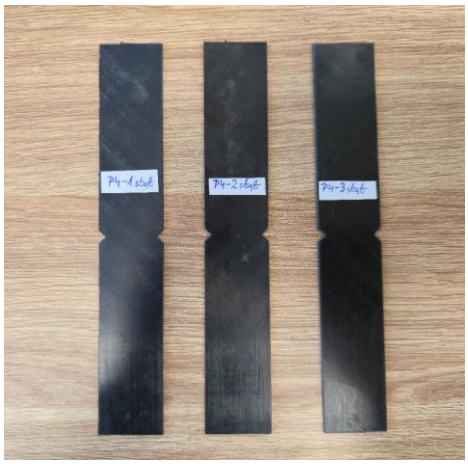
The visualization of the cross-section of the specimens shows irregularities in the fibers relative to the resin, and it is also worth mentioning that the specimens were cut from larger profiles using water jet technology.

As part of the experimental research, only a limited number of test specimens were available: three were prepared for static testing and three for fatigue testing. The small sample size

resulted from the agreed experimental conditions and the availability of test material. This should be taken into account when interpreting the obtained results. Despite the small number of specimens, particular attention was paid to ensuring the highest possible reproducibility of the experimental conditions and results. To this end, we applied a uniform methodology for specimen preparation, testing, and recording and analysis of results. All samples were tested under identical conditions whilst maintaining consistent test rig parameters, fixing method, loading procedure, and measurement and data acquisition method. Minimizing external factors and procedural variability increased the reliability of comparisons between results for individual samples. A sample size of three in each group does not permit a full assessment of the statistical variability of the phenomenon under investigation, nor can conclusions be drawn about the population with a high level of statistical confidence. The results should therefore be regarded primarily as a characterization of the behavior of the analyzed solution under the adopted experimental conditions. Maintaining methodological rigor and striving for maximum repeatability of the test procedure minimized the influence of random confounding factors, enhancing the cognitive value of the experiments.

3. Methodology for conducting experimental tests – static and fatigue

The conditions under which the fatigue and static tests were carried out were similar to those typically found in conventional laboratories. During the tests, the relative humidity was kept at around 50 percent, and the room temperature was maintained within the range of 22–23 °C. The experimental tests were conducted in two stages. The first stage involved typical static strength tests as part of a static tensile test. These tests were performed using a universal strength testing machine (Shimadzu AGXv2) with a maximum load capacity of 50,000 N. Dedicated Trapezium-V software was used for the static tests. Additionally, a standard video camera (1920×1080) recorded the tensile test, and a FLIR thermal imaging camera monitored the temperature distribution on the specimen surface throughout the experiment. Dedicated clamps (grips) were used to fix the test samples properly in position while ensuring axial tensioning. A modern strength testing machine with a high-precision sensor was used for the first stage of testing: static testing. The tests were conducted at room temperature with a traverse speed of 2 mm/min. Three test specimens were prepared as part of an experimental research project involving static tensile tests, as shown in Fig. 3. Figure 3 also illustrates a universal testing machine used for static testing. During static testing, we took particular care to ensure the specimens were properly attached; each specimen was attached 45 mm from the top and bottom edges.



(a)



(b)

Figure 3. First stage of experimental research: (a) specimens for static tests, (b) universal testing machine for static tests.

In the first stage of experimental research, we estimated the maximum loads at which the specimens were damaged using a static tensile test. The primary objective of the first stage of testing was to determine the limit loads at which the specimens were fractured. We then used this data in the next stage of testing, i.e., fatigue testing. Based on the estimated limit loads (i.e. the failure forces in the static tests), the range of loads acceptable

for further fatigue testing could be determined.

In the second stage of the research, the fatigue tests were carried out under loading conditions selected to prevent premature, complete fatigue failure. The aim of the fatigue testing was to observe the initial signs of damage in the low-cycle fatigue range without losing load-carrying capacity, i.e., to capture the initiation and evolution phase of damage in the composite material (initiation and further progressive damage were observed). The essence of fatigue testing, as part of the second stage of experimental research, was to analyze the behavior of composite structures within accepted fatigue testing parameters. The aim was to identify locally occurring signs of damage using independent non-destructive testing techniques. We conducted research on composite behavior under fatigue testing conditions using a specialized fatigue testing machine. Based on static tests, the desired fatigue test parameters were selected to prevent premature complete specimen failure while allowing observation of the initiation and progression of damage associated with low-cycle fatigue. The fatigue behavior of the specimens was analyzed primarily to assess damage initiation and evolution in the composite material. The fatigue testing was performed on an MTS Landmark 370 machine (servo-hydraulic machine with maximum load capacity 100,000 N) [45]. Based on preliminary static tests, the average static failure load was determined from three tests at 3830 N. Preliminary static tests enabled prediction of the maximum fatigue load range, helping ensure the fatigue tests were planned appropriately and that parameters were selected to capture both the first signs of damage and complete failure. The static tests determined the maximum fatigue load at which the specimen would fail, enabling estimation of a sufficient number of fatigue test cycles to ensure gradual failure of the composite structure while allowing progressive damage to be recorded up to loss of load-bearing capacity. Special hydraulic grips with a clamping pressure of 2,000 Psi (13.79 MPa) were used during fatigue testing. Fatigue testing was conducted using the MTS Flex Test™ 40 Station Manager software, which recorded and analyzed fatigue test data. The parameters evaluated during experimental testing with regard to fatigue response were as follows: F_{max} = 3,000 N (maximum load); F_{min} = 300 N (minimum load); F_m = 1,650 N (average load); F_a = 1,350 N (amplitude load); f = 10 Hz (frequency); R = 0.1 (the stress ratio). The loading frequency f was selected to prevent excessive heating of the specimens and to ensure that temperature changes during degradation could be measured using a thermography camera. The stress ratio was selected to investigate fatigue behavior in axial tension with minimum stress close to zero. For this reason, the most common case, R = 0.1, was selected. During fatigue testing, the specimens were initially tensioned to an average load value of F_m at a tensioning speed of 3,000 N/min. Fatigue testing used sinusoidal force excitation, with cycles characterized by tension and relaxation. Fig. 4 shows the specimens for fatigue testing and the fatigue testing machine.



(a)



(b)

Figure 4. Second stage of experimental research: (a) specimens for fatigue tests, (b) universal testing machine for fatigue tests.

During fatigue testing, particular care was taken to ensure the specimens were properly attached; each specimen was attached 45 mm from the top and bottom edges. The main aim of the fatigue tests was to detect any early indications of damage to composite structures. During fatigue testing, specimen elongation was recorded in real time, enabling the development of composite structure performance characteristics. The equivalent stiffness K (in N/mm) of the specimens was also determined during the tests using the quotient of the doubled amplitude of the applied load (F_{max}-F_{min}) and the specimen's elongation (u_{max}-u_{min}). The parameter representing the specimen's maximum elongation, u_{max}, was determined at the time point when the specimen reached its maximum load, F_{max}. The same approach was used to determine the minimum elongation. To minimize errors from factors such as sensor sampling frequency or the limited number of points, the equivalent stiffness K was determined over a specific cycle range in the n–m interval. The value of n-m interval was selected in such a way as to enable capturing the maximum and minimum force values for each iteration of the equivalent stiffness K. The chosen value (n-m = 50 cycles) is strongly related to the frequency of the applied loading and the data sampling frequency (force, displacement). The equivalent stiffness K of the specimen was determined using the following equation:

$$K(n-m) = \frac{F_{max}(n-m) - F_{min}(n-m)}{u_{max}(n-m) - u_{min}(n-m)} \quad (1)$$

Moreover, the dimensionless normalized stiffness (K_n) for the n–m cycle range was determined as follows:

$$K_n(n-m) = \frac{K(n-m)}{K_0(n_0)} \quad (2)$$

Parameter K_0 denotes the stiffness assumed as the initial stiffness (in N/mm and calculated for cycle n_0). For each specimen, K_0 was determined at the number of cycles n_0 corresponding to the point where the maximum fatigue load value stabilized. For the first specimen, the loading conditions stabilized after n_0 = 300 fatigue cycles. For the remaining samples, the load stabilized after n_0 = 50 cycles. The higher n_0 for the first specimen results from the testing machine's PID controller adapting to the specified loading conditions and the material being tested.

The degradation of the normalized stiffness (K_n) can be assumed to represent the specimen's cumulative damage. An initial normalized stiffness value of exactly 1 indicates an undamaged specimen. In practice, calculations start with a specified number of cycles rather than at the start of the machine. As the material degrades, the standardized stiffness value decreases. If $K_n = 0$, this corresponds to total failure of the test specimen. A steeper normalized stiffness curve indicates greater material degradation. The results from the above description will be presented in the research results section.

Several independent non-destructive testing methods were used during the experimental research to assess early signs of damage in the composite material. Passive thermography and acoustic emission were used simultaneously during the tests, while digital microscopy was used later. Passive thermography was used to analyze temperature changes in composite specimens during fatigue testing. We used both qualitative and quantitative assessments to identify areas susceptible to damage based on observed thermal changes, and we determined characteristics related to the course of these changes. The temperature gradient ΔT (difference between T_{max} maximum and T_{ref} reference temperatures) was recorded during the research:

$$\Delta T = T_{max} - T_{ref} \quad (3)$$

The temperature increment was evaluated as the difference between the temperature recorded at a given stage of the fatigue test and the initial temperature measured at the beginning of the test. Thus, the analysis was based on temperature changes relative to the initial thermal state rather than on absolute temperature values. We did not determine the specimens' emissivity experimentally. All measurements used the same material, surface condition, camera setup, and environmental conditions. Therefore, the infrared thermography analysis focused primarily on comparing temperature distributions and temporal temperature changes between regions rather than determining absolute temperature values. Emissivity uncertainty affects all measurements similarly and does not significantly influence the comparative analysis presented in this study.

Passive thermography studies were conducted using specialized equipment – an FLIR A325 thermal infrared camera [33,46] – Fig. 5. The dedicated software (IrNDT v1.7.2 and ThermaCAM Researcher Pro 2.10) enabled parameters to be

recorded in accordance with the settings: resolution 320 x 240 px; frame rate 1 Hz; spectral range 7.5–13 μm; temperature range -20 to +350 °C.

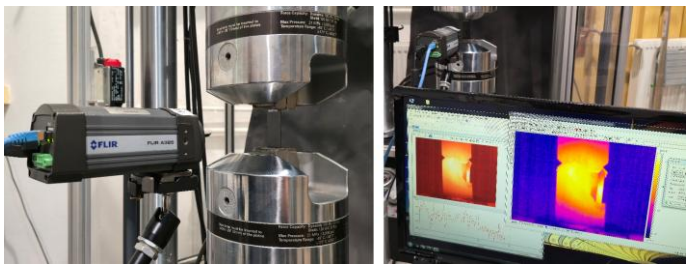


Figure 5. A system for conducting passive thermography tests.



Figure 6. A single-channel acoustic emission system.

Another device that supported non-destructive testing was the single-channel acoustic emission (AE) module SpotWave 201 [47] – Fig. 6. This device records test parameters in accordance with EN 13477-1 standard. The acoustic emission method detects and localizes elastic waves generated by internal processes in the material, such as fracturing or deformation. The acoustic emission system features the following optional technical parameters: sampling rate 2 MHz (16 bit); input range ±100 mV (100 dB_{AE}); analog filters (high-pass: 20 kHz 2nd order, low-pass 500 kHz 6th order); digital filters (butterworth IIR); power consumption 0.7 W (powered over USB 5V); ingress protection IP67; temperature range -20 to +60°C; weight 107 g. Fatigue testing was performed at a sampling frequency of 0.5 MHz. The test data were recorded using SpotWave Acquisition software, and the recorded data were analyzed and processed using VisualAE software. A dedicated piezoelectric sensor was used primarily to examine thin-walled composite materials designated VS150-L (passive piezoelectric AE sensor). The piezoelectric sensor, which was attached directly to the test specimens, had the following parameters: frequency range from 100 to 450 kHz; operating temperature from -50 to +100 °C; ingress protection rating IP40.

During the AE tests, the following parameters were recorded: amplitude, energy, and count. The reference value in the definition of AE amplitude is expressed in decibels. This is particularly important for the spotWave 201 from Vallen Systeme, as the device reports amplitude as dBAE rather than simply 'dB'. The amplitude signal A was recorded using the following equation:

$$A = 20 \cdot \log(ALIN) \tag{4}$$

Parameter A represents the peak amplitude of the burst signal, measured in dB_{AE} units. It is derived from the peak amplitude measurement in μV. *ALIN* represents the linear peak amplitude of the burst signal, and its resolution depends strictly on the measurement channel's input range. For an input range of 100 dB_{AE} (100 mV), the amplitude resolution is approximately 3.05 μV.

Regarding the acquisition/detection threshold, i.e., the minimum amplitude of the acoustic emission (AE) signal at which the SpotWave 201 recognizes the signal as an event ('hit') and records its parameters, this value is typically set to around 40 dB_{AE}. An AE measurement is triggered when the AE signal exceeds a user-defined detection threshold. This helps to reduce undesirable noise.

During acoustic emission testing, the most important signal is the energy signal E, which is determined using the following expression:

$$E = \Delta t \sum_{i=1}^{N} u_i^2 \tag{5}$$

Parameter E represents the energy signal of the burst signal originally expressed in eu units. The energy of the recorded signal is the sum of the squared voltage samples (u_i), beginning with the sample at the first threshold crossing ($i = 1$) and ending with the sample at which the duration discrimination time (*DDT*) has elapsed ($i = N$). The variable Δt represents the time difference between two consecutive voltage samples. Mathematically, conversion to actual true energy (*TE*) is performed as follows:

$$TE = \gamma \frac{1}{R} E \tag{6}$$

Coefficient γ corresponds to the conversion factor unit of eu to J and R to an ohmic resistance, in compliance with the following expressions:

$$\gamma = 10^{-14} \frac{V^2 s}{eu}, R = 10 k\Omega \tag{7}$$

The ohmic resistance of a device mainly depends on its input impedance. In general, the true energy result changes as the

input impedance changes. Since division by resistance constitutes a scaling factor, it is advisable to use arbitrary energy units and then convert them to engineering units. Although several different signals were recorded during the tests, only the energy signal was analyzed in depth.

Regarding the sensor's coupling conditions, the study used high-vacuum silicone grease (LOS 900-50) with a temperature range of -40 to +200 °C. The sensor was mounted directly onto the test specimen using a small aluminum profile to press its signal-recording surface against the specimen. Throughout the tests, direct contact between the sensor and the test specimen was ensured. The piezoelectric sensor was positioned so that its center lay within the vertical axis of symmetry of the test specimens, i.e. it was centered relative to their width. It was positioned so that the edge of the upper circular surface of the mounted sensor was at the same level as the lowest point of the notches. This ensured that the structure's behavior was not affected in the area of the notches themselves and that the structure was not stiffened at the notch locations. At the same time, the sensor was positioned at a safe distance from the clamps to avoid affecting the measurements.

Digital microscopy was employed in the final stage of non-destructive testing, particularly for the qualitative assessment of damage after fatigue testing. For this purpose, we used advanced testing equipment, primarily the VHX-970F microscope controller [47,48]. Microscopic examinations were conducted using a 20–200x magnification lens, as well as a system that allowed observation from different angles. We used an additional depth-of-field function to observe damage to composite specimens resulting from the tests. This function maintained high resolution within a larger microscopic field of view by using focus stacking with digital correction algorithms. The lens used in the research allowed images to be recorded with excellent telecentricity, i.e., the ability to keep the principal light rays parallel to the optical axis in the object and/or image space. This is crucial for digital microscopy systems, as well as for creating 3D (compositional) images and merging out-of-focus areas. Experimental tests using digital microscopy enabled detailed observation of defects, particularly after fatigue testing. Figure 7 shows the equipment used for digital microscopy testing.



Figure 7. Research equipment using digital microscopy.

All the above-mentioned equipment enabled comprehensive testing, including preliminary static and further fatigue testing. Independent non-destructive testing techniques made it possible to evaluate the results qualitatively and quantitatively.

4. Research results – static analysis

As part of the static strength tests, the load-carrying capacity of the structure was analyzed during static tensile testing. In the experimental tests conducted using a universal testing machine (Figure 8), the limit loads for three test specimens were determined. Figure 9 presents the static test results.

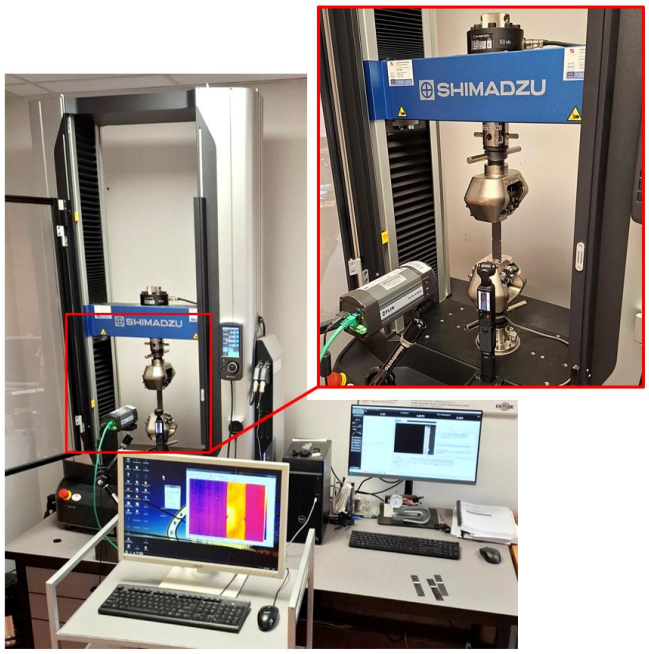


Figure 8. Static strength tests – an example of a research test presentation.

Based on the static tests, the failure load values were determined, enabling further fatigue testing on a fatigue testing machine in accordance with the appropriate test parameters. The limit load values were as follows: 4,131 N for specimen P4-1stat, 3,888 N for specimen P4-2stat, and 3,470 N for specimen P4-3stat. The average maximum load value was 3,830 N. The static test results are presented below as load versus displacement graphs, as shown in Fig. 9.

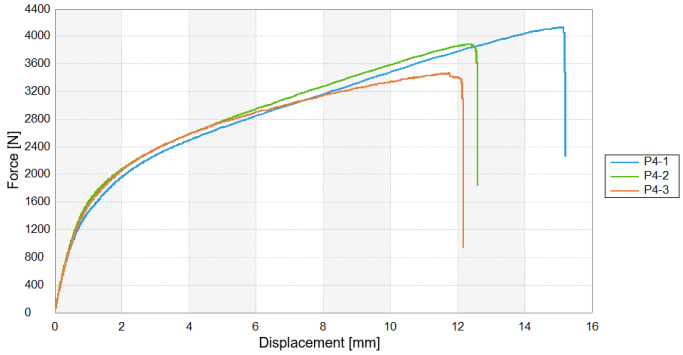


Figure 9. Relationships between tensile force and displacement recorded during static tensile tests.

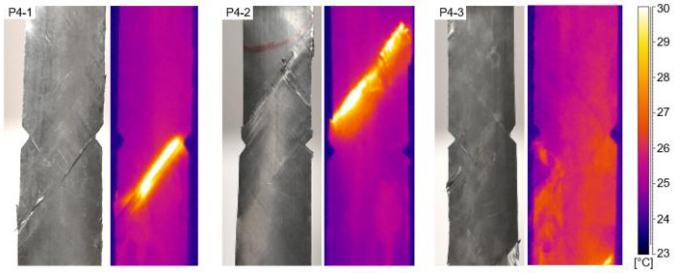
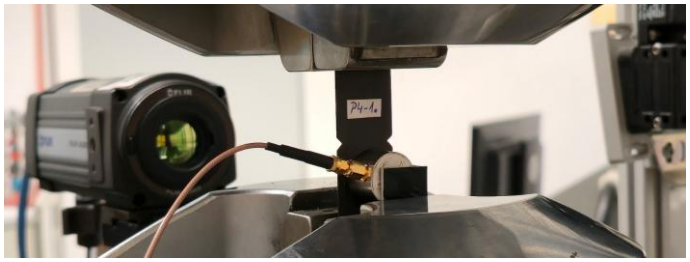


Figure 10. The failure forms for specimens P4-1, P4-2 and P4-3 recorded using a standard video camera and thermal infrared camera at the moment of final damage.

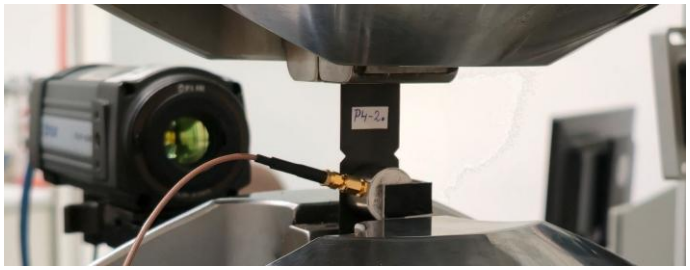
The tensile tests conducted on notched CFRP specimens revealed a characteristic sequence of damage development leading to final failure. The test progression was recorded simultaneously with a standard video camera and a thermal imaging camera, providing complementary insight into both the mechanical response and the material's thermographic signature. The thermal camera observations enabled clear identification of the final failure mode, capturing a pronounced localized temperature increase associated with the sudden energy release during the ultimate fracture event. This thermal hotspot corresponded spatially with the region of crack propagation initiated at the notch. The figure presents images from both the thermal and standard cameras at the moment of final failure, illustrating the correlation between the observed structural damage and the material's thermal response – Fig. 10.

5. Research results – fatigue analysis

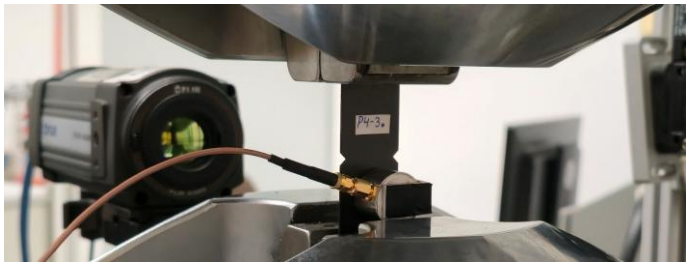
Based on fatigue testing, we identified the first signs of damage and failure in the composite specimens using both a fatigue machine and additional non-destructive testing techniques. Figure 11 shows the specimens during the experimental testing.



(a)



(b)



(c)

Figure 11. The specimens during fatigue testing: (a) P4-1, (b) P4-2, (c) P4-3.

Based on the data recorded by the software (force and displacement), it was possible to determine the equivalent normalized stiffness K_n. Both parameters are expressed in N/mm and illustrate the state of structural degradation of the specimens. In this context, we estimated characteristics representing 'stiffness degradation' by identifying a decrease in the equivalent stiffness K_n relative to the number of cycles. Figure 12 presents these characteristics.

Using the normalized stiffness changes in the samples, it was possible to estimate the average percentage damage level, among other things. Across the entire fatigue process, two

distinct stages with different rates of normalized stiffness degradation can be clearly identified. In the initial stage, which covers approximately 25-35% of the test, the degradation of K_n remains at a higher level. Based on the changes in normalized stiffness, damage initiation (e.g., delamination, fiber cracking, etc.) occurred at the very beginning of the fatigue test. In the second part of the test, the rate of degradation of K_n decreases and remains stable until complete fatigue failure. Based on the experimental tests, the average decrease in normalized stiffness at failure was estimated at approximately 35.62%. The decrease in the normalized stiffness for the individual specimens was as follows: 40.40% for P4-1, 32.15% for P4-2, and 34.32% for P4-3. The standard deviation was approximately 4.28%. This significant decrease in normalized stiffness after a relatively low number of fatigue cycles is due to the composite lay-up and the high fatigue loads applied in the tests. Figure 12 shows the number of cycles to failure (N_f) for each specimen.

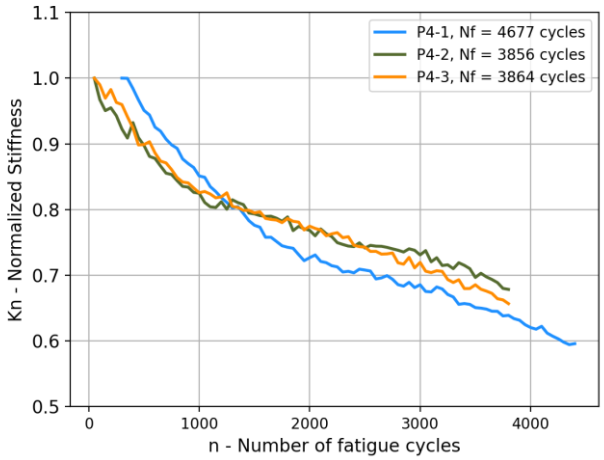


Figure 12. Change in normalized stiffness relative to the number of fatigue cycles.

From a scientific point of view, it was important to analyze the behavior of composite structures in relation to the recorded parameters. Several independent research results were recorded through low-cycle fatigue testing. We primarily recorded elongation (MTS), temperature gradient (ΔT), and acoustic emission energy signals (AE) in real time. For the temperature gradient, temperature change was recorded using the $\Delta T = T_{max} - T_{ref}$ function (where T_{max} is the maximum temperature and T_{ref} is the initial temperature recorded at the beginning of the fatigue test). Three regions of interest were defined for thermographic analysis: the left V-notch region, the right V-notch region, and the central specimen region. We used the same region dimensions and locations for all specimens. Figure 13 marks these regions.

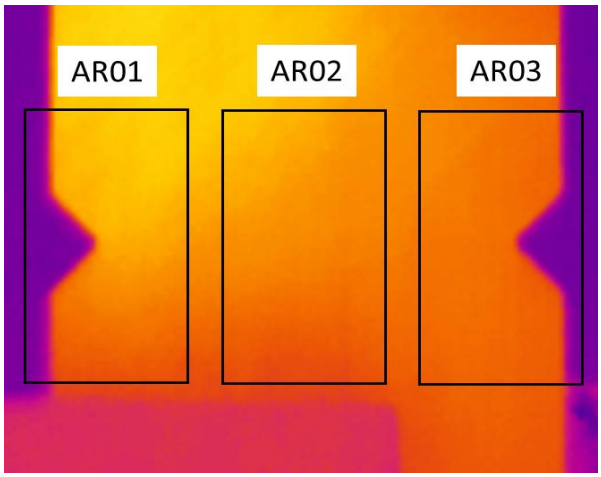
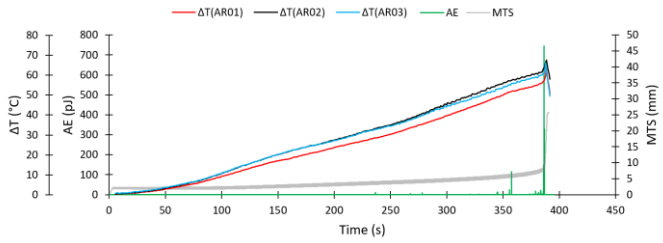


Figure 13. Separate research areas that were subjected to thermographic analysis.

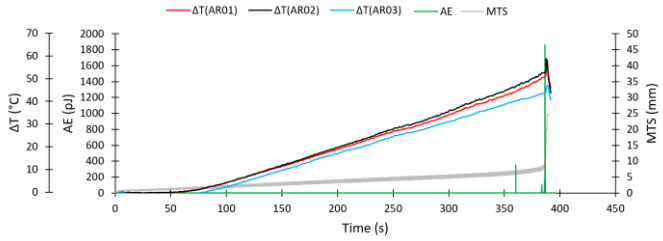
In the graphs (Figure 14), the elongation curve is marked in grey (MTS), the temperature gradient (ΔT) in red (AR01), black (AR02), and blue (AR03), and the acoustic emission energy signal in green (AE). In the first stage of fatigue testing, the specimen was tensioned only to the average fatigue load value. The second stage was the most important research stage, in which all signals were recorded: elongation, temperature gradient, and acoustic emission energy. Analysis of these signals enabled a quantitative assessment of the test results, particularly regarding signs of damage.

A qualitative comparison of the temperature-gradient evolution with the corresponding displacement response reveals a strong correlation between thermal and mechanical indicators of fatigue damage. The ΔT–time curve closely resembles a classical fatigue-damage progression curve, with a distinct initial stabilization stage followed by a gradual increase in the temperature gradient. This trend is particularly evident for specimens P4-2 and P4-3. For specimen P4-1, this effect is less visible due to the initial fatigue-test setup parameters. The onset of damage initiation, shown as a noticeable rise in the temperature increment at approximately 700 cycles (around 70 s), coincides well with observations of the fatigue-induced displacement increase in the specimens. Because Figure 14 uses vertical scales to present combined MTS, AE, and thermographic results, these early changes are not clearly visible. Progressive increases in ΔT correspond to stiffness

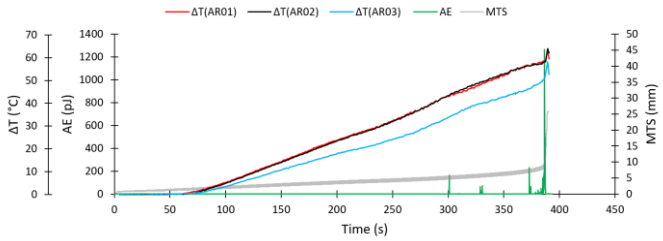
degradation (Figure 12). Comparing displacement and temperature responses indicates that both thermographic and mechanical measurements consistently capture local energy-dissipation mechanisms. In acoustic emission signal analysis, we observed similarities among the analyzed test specimens. The acoustic emission energy signal showed local peaks (increases) before the maximum increase at the point of loss of load capacity. Examining the specimens revealed local energy increases (exceeding 100 pJ), which correspond to the initiation of damage in the composite material due to fatigue testing. For specimens P4-1 and P4-2, these increases were observed after 350 s, whereas for specimen P4-3, this occurred after just 300 s. Naturally, the maximum signal increase was recorded during the final phase of acoustic emission energy signal recording, corresponding to the material's failure.



(a)



(b)



(c)

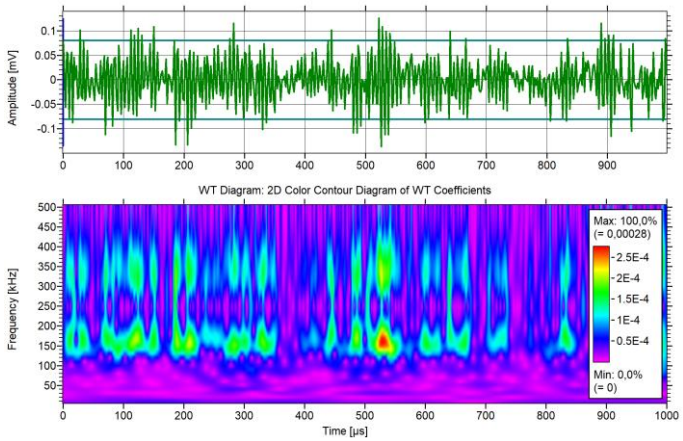
Figure 14. Experimental characteristics showing the course of temperature (increase) change, acoustic energy signal and elongation of the composite structure: (a) P4-1, (b) P4-2, (c) P4-3.

For the acoustic emission method, we used an additional wavelet-transform-based test to identify early mechanical damage. The analyses were performed on data obtained directly from acoustic emission (based on the *.tradb file obtained from the equipment – transition data). Significant signal changes corresponding to mechanical damage to the composite material structure were presented using wavelet transform (WT). WT was used to analyze non-stationary signals where frequency and amplitude characteristics change in real time. WT provides information about time-frequency changes in signals. WT determines the frequency spectrum over time using short 'wavelet' segments of the waveform as basic functions [49–51]. The WT graph shows the wavelet transform values in rainbow colors on an automatic scale. Lower values (close to or equal to zero) correspond to pink, while peak values correspond to red, as indicated in the figure legends. Figure 15 shows example results obtained using WT. These results are presented at points where significant peaks occurred in the acoustic emission signal during fatigue testing. The results cover a relatively short period of time. Acoustic emission (AE) testing uses wavelet transform (WT) coefficients to analyze signals in the time-frequency domain. This provides a more detailed representation than traditional methods such as the Fast Fourier Transform (FFT). WT coefficients provide information about a signal's energy at different frequencies and times. This enables identification of different types of damage, as well as separating signals from noise and characterizing transient events. WT coefficients also enable the identification of wave modes, determining arrival times and classifying AE events.

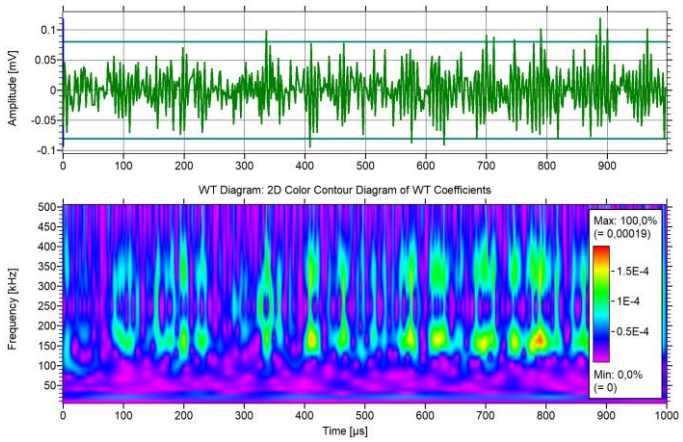
The sensor's resonant frequency is 150 kHz, at which point it achieves maximum sensitivity. As resonance amplifies the mechanical signal, waves around 150 kHz generate the highest output voltage. This makes weak acoustic emission signals, such as those caused by microcracks in composites, easier to detect. With a frequency response range of 100–450 kHz, the Vallen VS150-L sensor can effectively detect acoustic waves within this band. Frequencies below 100 kHz are excluded to minimise the impact of mechanical and ambient noise, and frequencies above 450 kHz are not as useful due to the material's rapid damping properties.

Papers [52–56] describe damage-mechanism identification in composite materials and provide a partial assessment of the predominant forms of damage in given frequency bands. This is

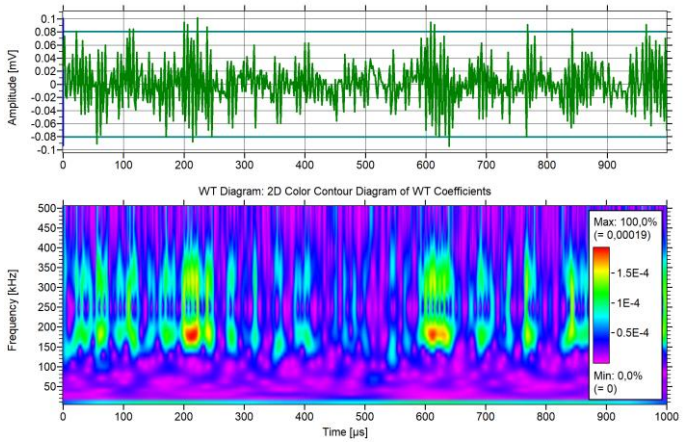
demonstrated in the frequency-time plots derived from the wavelet transform.



(a)



(b)



(c)

Figure 15. Wavelet transform – WT contour plot and transient waveform: (a) specimen P4-1, (b) specimen P4-2, (c) specimen P4-3.

Notably, regardless of the damage mechanism, local maximum-energy signals occurred at approximately 150 kHz. The WT coefficient changes show considerable regularity. This is because low-cycle fatigue tests reveal local symptoms of material damage. WT characteristics were presented using relatively short time intervals. The WT coefficients in the time-frequency characteristics were relatively similar. Despite the short analysis period, progressive damage was observed during the fatigue tests (WT coefficient intensity was monitored). A brief interpretation of the results is provided for several frequency ranges. The 120–200 kHz range is the dominant range associated with epoxy matrix fracture and the progression of interlayer delamination. The highest signal activity indicates the rapid progression of these defects. In the>250 kHz range, higher-frequency pulses indicate localized damage and partial fracture of the carbon fibers. At frequencies <100 kHz, low activity corresponds to the early stages of microcracking and the effects of wave propagation or friction within the material. The $[45/-45/45/-45]_s$ lay-up favors shear stresses; therefore, the intense activity observed in the 120–200 kHz range is consistent with this laminate's behavior. The absence of strong dominance of the highest frequencies suggests that complete fiber failure was not the dominant mechanism in the analyzed signal segment. The frequency ranges in which the failure types described in this paper typically occur have been partially documented in scientific publications referenced before the wavelet transform figures [52–56]. It should be noted that, depending on the type of test, different forms of failure may occur at different frequencies in the case of static, fatigue, or dynamic tests. Papers [50,51] present a detailed description that enables interpretation of the obtained characteristics. A more effective approach would be to analyse the following three parameters simultaneously: frequency, occurrence time and WT coefficient energy. Further research will focus on this approach. Temperature monitoring during fatigue loading provides valuable insight into the degradation processes occurring in composite laminates. The progressive increase in surface temperature reflects local energy dissipation associated with internal friction, matrix cracking, fiber–matrix debonding, and shear-driven deformation mechanisms. In this study, passive infrared thermography was used to monitor composite specimens with notches. The specimens P4-1, P4-2, and P4-3 were manufactured exclusively from $[45/-45/45/-45]_s$ plies, a configuration that strongly governs shear-dominated damage mechanisms and influences the directionality of fatigue

degradation. We defined three regions of interest (Figure 13): AR01 (left notch), AR02 (central region), and AR03 (right notch). AR02, located away from the stress concentrators, was used to assess the laminate's intrinsic thermal response, whereas AR01 and AR03 enabled tracking of damage initiation and propagation in the notched zones. Figure 16 presents the evolution of surface temperature as a function of the number of cycles. Thermographic data were acquired at 1 Hz, with a time-to-cycle conversion factor of 10. All specimens were loaded to failure under constant amplitude fatigue conditions. The $[45/-45/45/-45]_s$ laminates exhibited abrupt final failure, which limited the ability to observe gradual degradation in detail. Nevertheless, the thermographic sequences revealed distinct features of the damage process. Degradation progressed along the $[45/-45/45/-45]_s$ fiber bands and was primarily associated with matrix-dominated mechanisms, followed by fiber separation and sliding along the fiber paths. Damage initiated in the notch area for all specimens, and initiation consistently occurred beyond approximately 700 cycles. Specimens P4-1 and P4-3 exhibited substantially higher apparent energy release at failure than P4-2, consistent with more localized and rapid damage accumulation.

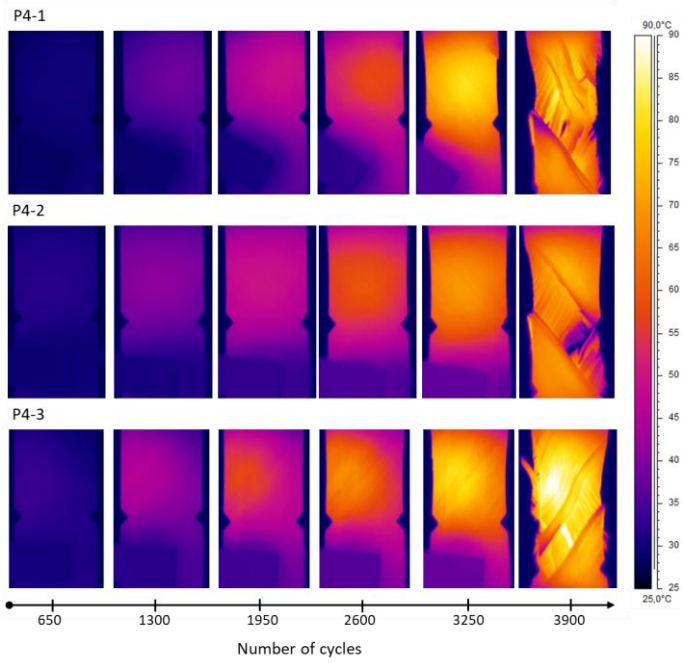
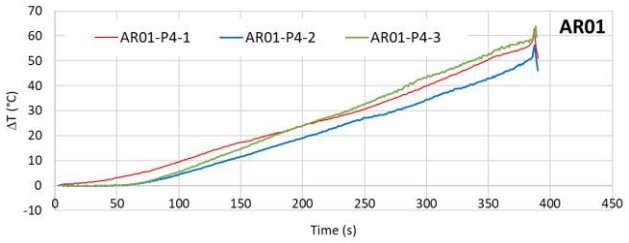


Figure 16. Thermographic sequence illustrating the evolution of surface temperature during fatigue loading for specimens P4-1, P4-2, and P4-3.

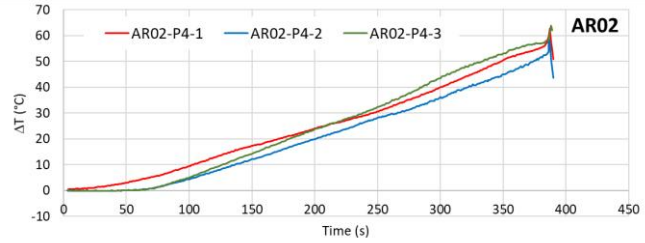
The thermal response revealed a pronounced asymmetry in damage development. In specimens P4-1 and P4-3, degradation localized near a single dominant notch—the right-hand notch in P4-1 and the left-hand notch in P4-3. This behavior likely resulted from slight specimen misalignment during gripping, which introduced asymmetric bending or shear components and consequently affected the local stress distribution. In contrast, specimen P4-2 exhibited a more balanced contribution from both notches. Its temperature field remained nearly symmetric across the specimen width, indicating a more uniform load transfer and a more homogeneous pattern of damage progression. As a result, its global surface temperature at failure was approximately 10°C lower than that of P4-1 and P4-3, reflecting a less abrupt and less energetic failure event. However, misalignment is not the only probable source of asymmetry. In addition, differences in notch geometry, local fiber waviness, and micro-scale variations in laminate thickness may further contribute to non-uniform stress fields. The shear-dominated behavior of $[45/-45/45/-45]_s$ laminates strengthens such imperfections.

Figure 17 reports the temperature increase ΔT for the selected areas. A clear distinction between the notches is evident and is consistent with the asymmetric behavior of the two specimens: the right-hand area AR03 dominated the early damage evolution in specimen P4-1, whereas the left-hand area AR01 governed the fatigue behavior of specimen P4-3. The thermal response in the central region AR02 was similar in both specimens, while specimen P4-2 consistently exhibited lower ΔT in this region, reflecting a more uniform load distribution across the width.

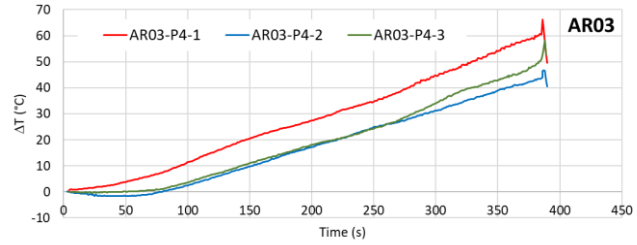
These observations highlight the strong influence of the $[45/-45/45/-45]_s$ configuration. Because this configuration is shear-dominated, any deviation from axial loading is amplified in the thermographic response. Even small misalignment errors introduce local bending or asymmetric shear components, thus shifting the position of damage initiation and accelerating degradation on one side of the specimen. Eliminating such effects improves the uniformity of the stress field, delays damage initiation, and moderates the thermal response during fatigue loading. The fatigue behavior of specimen P4-2 confirms this: with minimal misalignment, damage progression was more gradual, and the temperature increase remained stable, leading to a less dynamic final failure.



(a)

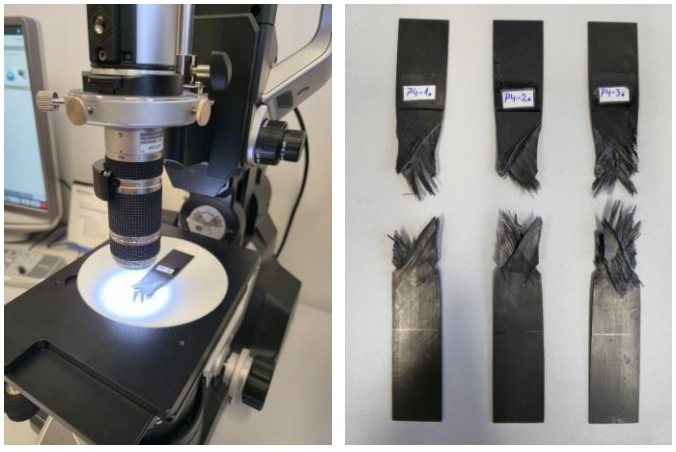


(b)



(c)

Figure 17. Temperature increase ΔT in regions: (a) AR01, (b) AR02, and (c) AR03.

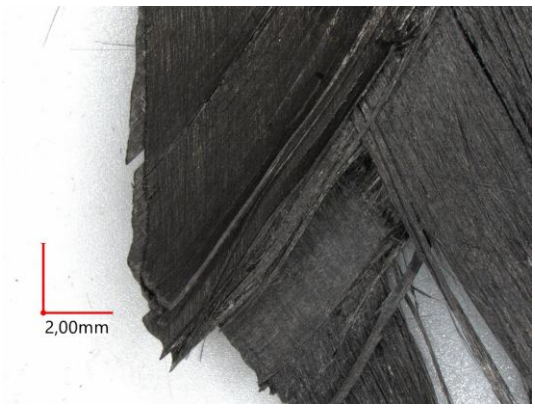


(a) (b)

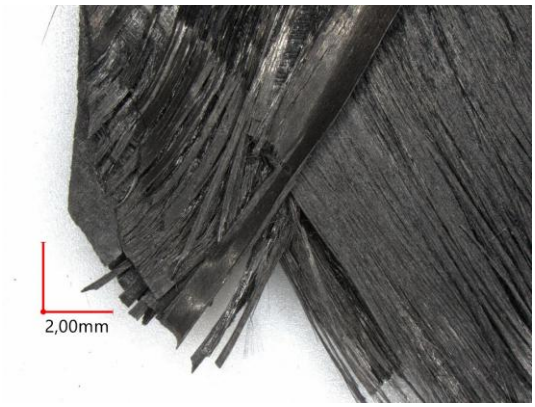
Figure 18. Microscopic analyses: (a) specimen under observation, (b) specimens after fatigue testing.

The final stage of the research involved making microscopic observations. These analyses were performed using digital microscopy. The three specimens subjected to fatigue testing exhibited similar behavior during the process of damage. Figure 18 presents the results.

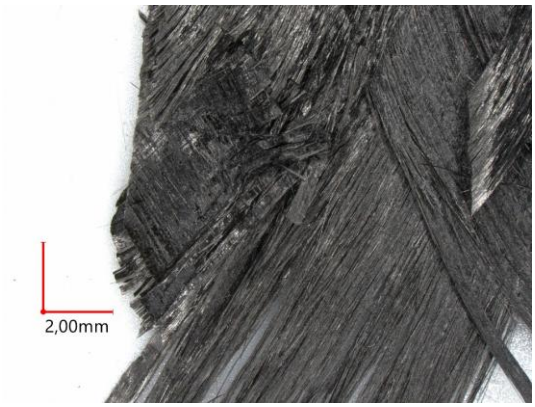
Microscopic observations revealed extensive damage to the composite structures in the specimen's central region. During testing, the specimens demonstrated significant elongation and narrowing in the central area. The $[45/-45/45/-45]_s$ composite lay-up (layer arrangement) caused the specimen to elongate significantly during fatigue testing, accompanied by narrowing. The test specimens showed extensive damage at the moment of failure during fatigue testing – Figure 19.



(a)



(b)



(c)

Figure 19. Graphical representation of the damaged area (mid-left section): (a) P4-1, (b) P4-2, (c) P4-3.

The damage was extensive, with both layer fracturing (fiber bond breakage) and delamination. We used the depth-of-field

option during microscopic observation to improve visualization of the damage. This study enabled both quantitative and qualitative assessments within its scope.

Some uncertainty may have arisen during the tests regarding specimen clamping and alignment in the jaws of the fatigue testing machine. Despite taking due care when mounting the specimens, slight deviations from ideal coaxial alignment may have occurred during clamping. This type of misalignment can lead to variations in stress and strain distribution, which may slightly influence the asymmetrical progression of damage observed during fatigue and thermographic testing.

This phenomenon should be regarded as a limitation of the experimental method. As it is not possible to quantify the effect of minor alignment deviations on each specimen precisely, this uncertainty has not been included as a separate component of the measurement uncertainty. Nevertheless, we consider the potential influence of misalignment minimal and not affecting the validity of the main observations or conclusions drawn from the studies. Accordingly, we included this information in the manuscript as an experimental limitation and a possible source of slight asymmetry in damage development.

6. Discussion

The conducted experiments enabled fatigue damage progression in notched CFRP laminates with the stacking sequence $[45/-45/45/-45]_s$ to be evaluated using complementary measurement techniques, including mechanical response analysis, passive infrared thermography, acoustic emission (AE), wavelet transform (WT) analysis, and microscopic observations. Together, these methods provide a multi-scale assessment of degradation processes during fatigue loading. The results show that each technique captures different aspects of damage evolution and that comprehensive interpretation is possible only when the methods are analyzed together.

One of the most consistent correlations between stiffness degradation and thermographic results was the relationship between normalized stiffness degradation and temperature evolution. All specimens exhibited a comparable reduction in stiffness, with decreases ranging from approximately 32% to 36%. Simultaneously, the thermographic measurements showed a gradual temperature increase that coincided with the accelerated degradation identified from the mechanical response. The correspondence between stiffness degradation and temperature evolution suggests that both parameters reflect the accumulation of internal damage mechanisms, including matrix cracking, fiber-matrix interface degradation, and delamination. Although no dedicated emissivity calibration was performed, its influence on the main conclusions is considered limited because all specimens were manufactured from the same material, tested under identical conditions, and evaluated primarily based on relative temperature changes rather than absolute temperature values.

Acoustic emission measurements accompanied the thermographic observations by providing information on discrete damage events occurring throughout fatigue loading. High-energy AE events were recorded before final failure and generally coincided with periods of accelerated thermal activity and stiffness degradation. However, a direct one-to-one correlation between AE peaks and temperature increases was not always observed. This is expected because acoustic emission is sensitive to individual damage events, whereas thermography reflects cumulative energy dissipation associated with progressive material degradation. Consequently, the two techniques should be regarded as complementary rather than directly equivalent diagnostic tools.

Wavelet-transform analysis improved the interpretation of the AE signals by enabling identification of dominant frequency bands associated with different damage stages. The frequency characteristics observed in the present study are consistent with the fatigue behavior commonly reported for ±45° CFRP laminates by Lei et al. [57], where the load is transferred primarily through in-plane shear stresses. In such laminates, fatigue damage typically arises from matrix cracking, fiber-matrix debonding, interlaminar shear cracking, and progressive delamination rather than immediate fiber rupture. Previous studies have shown that off-axis CFRP laminates exhibit substantial stiffness degradation due to the gradual accumulation of matrix-dominated damage mechanisms and interfacial failure processes [58,59].

Microscopic observations revealed extensive matrix degradation, fiber separation, and delamination near the notch, which corresponded well with locations of elevated thermal activity and increased AE response. These observations agree with previous investigations of ±45° CFRP laminates, where

fatigue damage initiates through distributed matrix cracking and interface debonding, followed by delamination growth and local fiber pull-out or fiber fracture during the final stages of failure [59]. Agreement among thermography, acoustic emission, WT analysis, and microscopy significantly increases confidence in the interpretation of the observed damage evolution.

Some variability between specimens was observed, particularly regarding the symmetry of damage development around the notches. Small differences in gripping conditions, specimen alignment, local geometric imperfections, or manufacturing-induced material heterogeneity may have influenced the local stress distribution and contributed to the observed differences in thermal and AE responses.

Overall, the combined application of thermography, acoustic emission, wavelet-transform analysis, and microscopic observations provided a comprehensive description of fatigue damage evolution in notched ±45° CFRP laminates. The strongest correlation was observed between stiffness degradation and thermographic evolution, both indicating the beginning of progressive fatigue damage. Acoustic emission detected discrete damage events earlier, while WT analysis improved interpretation of the underlying failure mechanisms. Post-failure microscopy confirmed the predominance of matrix cracking, delamination, and fiber separation. The combined use of mechanical measurements, passive thermography, acoustic emission, and microscopy therefore proved highly effective for characterizing the fatigue degradation of notched CFRP laminates.

7. Conclusion

The combined use of infrared thermography, AE, and displacement measurements proved effective for identifying both the initiation and progression of fatigue damage in ±45° composite laminates. The general conclusions are as follows:

- As a result of preformed tensile static specimen tests P4-1, P4-2, and P4-3, the following static failure forces were obtained, namely: 4,131 N, 3,888 N, and 3,470 N, respectively. Thus, the average failure force is equal to 3,830 N. The displacements corresponding to the failure forces are significant, exceeding 12 mm for specimen P4-3 and 14 mm for P4-1 (Fig. 9).
- The damage mechanism observed in the investigated structures develops predominantly along the fiber direction. The combined thermographic and visual observations suggest that matrix cracking, fiber-matrix debonding, and progressive delamination are the dominant damage mechanisms during fatigue loading. These processes may promote local fiber displacement and load redistribution within the damaged matrix. As shown in Fig. 10, the regions of increased temperature identified by thermography correspond well with the visible damage observed in photographs captured using a conventional camera. Although the experimental observations indicate that matrix-dominated damage governs the degradation process, the presence of local fiber fracture cannot be excluded without detailed high-magnification fractographic analysis.
- For tracing the damage evolution, the acoustic signal was registered. Moreover, the wavelet transform was applied to the registered signals. The analysis of the magnitude of the wavelet coefficients enables the estimation of the damage growth inside the studied specimens (Fig. 15). In the $[45/-45/45/-45]_s$ laminate lay-up under investigation, the predominant failure mechanisms are matrix cracking and delamination, whilst fiber damage occurs at a later stage of material degradation.
- During the fatigue tests, the temperature evolution in the region between the notches exhibited a characteristic three-stage behavior rather than a linear increase with the number of load cycles (Fig. 17). An initial temperature stabilization phase was followed by a gradual temperature rise associated with progressive material degradation, and finally by a rapid temperature increase immediately preceding specimen failure. A similar trend was observed in the displacement response, with an accelerated growth occurring during the final stage of fatigue life.
- The principal limitation of the present study is the relatively small number of specimens. While the results obtained from the three tested laminates consistently indicate similar degradation pathways and failure mechanisms, the dataset does not permit rigorous statistical assessment of variability or quantitative validation of correlations between individual monitoring

parameters. Therefore, interpret the identified relationships primarily as indications of underlying damage mechanisms rather than statistically validated correlations.

- Future studies involving a larger experimental dataset would allow the statistical assessment of variability and improve the reliability of multimodal approaches for fatigue damage monitoring in CFRP structures.

References

1. Suresh S. *Fatigue of Materials*. Cambridge University Press; 1998.
2. Stephens RI, Fatemi A, Stephens RR, Fuch HO. *Metal Fatigue in Engineering*. Wiley; 2000.
3. Harris B. *Fatigue in Composites: Science and Technology of the Fatigue Response of Fibre-Reinforced Plastics*. Woodhead Publishing; 2003.
4. Talreja R, Singh CV. *Damage Failure of Composite Materials*. Cambridge University Press; 2012.
5. Reifsnider KL, Case SW. *Damage Tolerance and Durability of Material Systems*. Wiley; 2002.
6. Liu Y, Xie J, Chen X. Characterization of progressive damage behaviour and failure mechanism of carbon fiber reinforced composite laminates. *Scientific Reports* 2025; 13791. https://doi.org/10.1038/s41598-025-98774-7.
7. Stinchcomb WW, Reifsnider KL. *Fatigue Damage Mechanisms in Composite Materials*: *A Review*. Fatigue Mechanisms (JT Fong); 1979.
8. Chandran KSR. Review: Fatigue of Fiber-Reinforced Composites, Damage and Failure. *Journal of the Indian Institute of Science* 2022; 102(1): 439-460. https://journal.iisc.ac.in/index.php/iisc/article/view/4969.
9. Wang Z, Zhang N, Wang Q. Tensile behaviour of open-hole and bolted steel plates reinforced by CFRP strips. *Composites Part B: Engineering* 2016; 100: 101-113. http://dx.doi.org/10.1016/j.compositesb.2016.06.038.
10. Mu PG, Wan XP, Zhao MY. A New Approach to Fatigue Damage Modeling of Composite Laminates. *Advanced Materials Research* 2011; 338: 315-318. https://doi.org/10.4028/www.scientific.net/AMR.338.315.
11. Samborski S. Numerical analysis of the DCB test configuration applicability to mechanically coupled Fiber Reinforced Laminated Composite beams. *Composite Structures* 2016; 152: 477-487. http://dx.doi.org/10.1016/j.compstruct.2016.05.060.
12. Romanowicz P, Muc A. Estimation of Notched Composite Plates Fatigue Life Using Residual Strength Model Calibrated by Step-Wise Tests. *Materials* 2018; 11(11): 2180. https://doi.org/10.3390/ma11112180.
13. Muc A, Chwał M, Romanowicz P, Stawiarski A. Fatigue-Damage Evolution of Notched Composite Multilayered Structures under Tensile Loads. *Journal of Composite Science* 2018; 2(2): 27. https://doi.org/10.3390/jcs2020027.
14. Aidi B, Philen MK, Case SW. Progressive damage assessment of centrally notched composite specimens in fatigue, *Composites Part A: Applied Science and Manufacturing* 2015; 74: 47-59. http://dx.doi.org/10.1016/j.compositesa.2015.03.022.
15. Saidulu H, Manzoor Hussain M. Flexural Fatigue Analysis of Fiber Reinforced Composite Laminates. *International Journal of Mechanical Engineering and Technology* 2018; 9(1): 68-74. http://iaeme.com/Home/issue/IJMET?Volume=9&Issue=1.
16. Quaresimin M, Susmel L, Talreja R. Fatigue behaviour and life assessment of composite laminates under multiaxial loadings. *International Journal of Fatigue* 2010; 32(1): 2-16. https://doi.org/10.1016/j.ijfatigue.2009.02.012.
17. Hofman P, van der Meer FP, Sluys LJ. Modeling of Progressive High-Cycle Fatigue in Composite Laminates Accounting for Local Stress Ratios. *Composites Part A: Applied Science and Manufacturing* 2024; 183: 108219. https://doi.org/10.1016/j.compositesa.2024.108219.
18. Lee CS, Hwang WB, Park HC, Han KS. Fatigue Failure Model for Composite Laminates under Multi-Axial Cyclic Loading. *Key Engineering Materials* 2000; 183-187: 945-950. https://doi.org/10.4028/www.scientific.net/KEM.183-187.945.
19. Lai J, Xia Y, Huang Z, Liu B, Mo M, Yu J. Fatigue life prediction method of carbon fiber-reinforced composites. *e-Polymers* 2024; 24: 1. https://doi.org/10.1515/epoly-2023-0150.
20. Cheng ZQ, Tan W, Xiong JJ, Hed EM, Wang YP. Modelling Fatigue Behaviours and Lifetimes of Novel GLARE Laminates under Random Loading Spectrum. *Composite Structures* 2023; 311: 116799. https://doi.org/10.1016/j.compstruct.2023.116799.
21. Deng J, Zhou J, Wu T, Liu Z, Wu Z. Review and Assessment of Fatigue Delamination Damage of Laminated Composite Structures. *Materials* 2023; 16: 7677. https://doi.org/10.3390/ma16247677.
22. Khan S, Rahimian Koloor S, King Jye W, Siebert G, Tamin M. A Fatigue Model to Predict Interlaminar Damage of FRP Composite Laminates Subjected to Mode I Load. *Polymers* 2023; 15(3): 527. https://doi.org/10.3390/polym15030527.

23. Kumagai S, Shindo Y. Experimental and Analytical Evaluation of the Notched Tensile Fracture of CFRP-Woven Laminates at Low Temperatures. *Journal of Composite Materials* 2004; 38(13): 1151-1164. https://doi.org/10.1177/0021998304042080.
24. Gahleitner L, Thummerer G, Reitinger B, Meirer K, Mayr G. 3D photothermal reconstruction of subsurface defects in notched multidirectional CFRP laminates due to tensile fatigue loading, *NDT & E International* 2022; 131: 102702. https://doi.org/10.1016/j.ndteint.2022.102702.
25. Serra J, Grotto F, Castanié, Bouvet C. Compared behaviour of notched thermoplastic and thermoset carbon reinforced panels under multiaxial loadings. *Composite Structures* 2026; 390: 120475. https://doi.org/10.1016/j.compstruct.2026.120475.
26. Mahesh P, Chinthapenta V, Raju G, Ramji M. Experimental investigation on open-hole CFRP laminate under combined loading using acoustic emission and digital image correlation. *Theoretical and Applied Fracture Mechanics* 2024; 130: 104300. https://doi.org/10.1016/j.tafmec.2024.104300.
27. Arumugam V, Naren Shankar R, Sridhar B, A. Joseph Stanley. Ultimate Strength Prediction of Carbon/Epoxy Tensile Specimens from Acoustic Emission Data. *Journal of Materials Science & Technology* 2010; 26(8): 725-729. https://doi.org/10.1016/S1005-0302(10)60114-4.
28. Kotsikos G, Evans JT, Gibson AG, Hale J. Use of acoustic emission to characterize corrosion fatigue damage accumulation in glass fiber reinforced polyester laminates. *Polymer Composites* 2004; 20(5): 689-696. https://doi.org/10.1002/pc.10392.
29. Panasiuk K, Dudzik K, Hajdukiewicz G. Acoustic Emission as a Method for Analyzing Changes and Detecting Damage in Composite Materials During Loading. *Archives of Acoustics* 2021; 46(3): 399-407. https://doi.org/10.24425/aoa.2021.138133.
30. Muflikhun MA, Fiedler B. Non-destructive testing of CFRP laminates for aerospace structures: Acoustic emission and ultrasonic longitudinal wave (ULW) evaluation under Mode II loading with destructive validation. *Results in Engineering* 2026; 30: 110850. https://doi.org/10.1016/j.rineng.2026.110850.
31. Katunin A. Thermal fatigue of polymeric composites under repeated loading. *Journal of Reinforced Plastics and Composite* 2012; 31(15): 1037-1044. https://doi.org/10.1177/0731684412452679.
32. Katunin A. Fatigue of polymeric composites during stationary and non-stationary self-heating. *Composites Theory and Practice* 2018; 18(1): 19-24.
33. Stawiarski A, Chwal M, Barski M, Augustyn M. The wrinkles characterization in GFRP composites by infrared active thermography. *Materials* 2023; 16: 4236. https://doi.org/10.3390/ma16124236.
34. Romanowicz P, Szybiński B, Wygoda M. Assessment of Digital Image Correlation Effectiveness and Quality in Determination of Surface Strains of Hybrid Steel/Composite Structures. *Materials* 2024; 17(14): 3561. https://doi.org/10.3390/ma17143561.
35. Wang Y, Chen Q, Luo Q, Li Q, Sun G. Characterizing damage evolution in fiber reinforced composites using in-situ X-ray computed tomography, deep machine learning and digital volume correlation (DVC). *Composites Science and Technology* 2024; 254: 110650. https://doi.org/10.1016/j.compscitech.2024.110650.
36. Helizanowicz B, Helizanowicz D, Krzemiński, Matula G. Use of computed tomography to assess quality and structure of curved CFRP laminate samples produced by autoclave technology. *Composites Theory and Practice* 2024; 24(1): 72-77. https://doi.org/10.62753/ctp.2024.10.1.1.
37. Heuer H, Schulze M, Pooch M, Gäbler S, Nocke A, Bardl G, Cherif Ch, Klein M, Kupke R, Vetter R, Lenz F, Kliem M, Bülow C, Goyvaerts J, Mayer T, Petrenz S. Review on quality assurance along the CFRP value chain – Non-destructive testing of fabrics, preforms and CFRP by HF radio wave techniques. *Composites Part B: Engineering* 2015; 77: 494-501. http://dx.doi.org/10.1016/j.compositesb.2015.03.022.
38. Dong B, Zhao R, Li H, Li J, Yu K. Nonlinear thermal vibration of pyramidal-truss cellular cylindrical shells. *International Journal of Mechanical Sciences* 2026; 326: 111872. https://doi.org/10.1016/j.ijmecsci.2026.111872.
39. Dong B, Li T, Zhao R, Li J, Yu K. Vibration and response characteristics of variable stiffness composite plates enveloping piezoelectric panels with arbitrary cutouts: a unified discretization modelling framework. *Composite Structures* 2026; 387: 120286. https://doi.org/10.1016/j.compstruct.2026.120286.
40. Dong B, Zhao R, Liu Z, Zhang L, Yu K, Li J. Nonlinear combined vibration modeling and analysis of honeycomb-filled corrugated core cylindrical shells considering thermal effects. *Thin-Walled Structures* 2026; 219: 114257. https://doi.org/10.1016/j.tws.2025.114257.
41. Feng J, Gao C, Safaei B, Qin Z, Wu H, Chu F, Scarpa F. Exceptional damping of CFRPs: Unveiling the impact of carbon fiber surface

treatments. *Composites Part B: Engineering* 2025; 290: 111973. https://doi.org/10.1016/j.compositesb.2024.111973.

42. Feng J, Safaei B, Qin Z, Chu F. Nature-inspired energy dissipation sandwich composites reinforced with high-friction graphene. *Composites Science and Technology* 2023; 233: 109925. https://doi.org/10.1016/j.compscitech.2023.109925.
43. Rozylo P, Smagowski W, Pasnik J. Experimental Research in the Aspect of Determining the Mechanical and Strength Properties of the Composite Material Made of Carbon-Epoxy Composite. *Advances in Science and Technology – Research Journal* 2023; 17(2): 232-246. https://doi.org/10.12913/22998624/161598.
44. Debski H, Samborski S, Rozylo P, Wysmulski P. Stability and Load-Carrying Capacity of Thin-Walled FRP Composite Z-Profiles under Eccentric Compression. *Materials* 2020; 13: 2956. https://doi.org/10.3390/ma13132956.
45. Romanowicz PJ, Szybinski B, Wygoda M. Fatigue performance of open-hole structural elements reinforced by CFRP overlays. *International Journal of Adhesion & Adhesives* 2024; 130: 103606. https://doi.org/10.1016/j.ijadhadh.2023.103606.
46. Stawiarski A. The non-destructive evaluation of the GFRP composite plate with an elliptical hole under fatigue loading conditions. *Mechanical Systems and Signal Processing* 2018; 112: 31-43. https://doi.org/10.1016/j.ymssp.2018.04.022.
47. Rozylo P. Study of the behavior of thin-walled composite structures with closed sections under three-point bending tests. *Advances in Science and Technology – Research Journal* 2025; 19(6): 403-413. https://doi.org/10.12913/22998624/203459.
48. Roslaniec K, Rozylo P. Influence of composite lay-up on the load-carrying capacity of structures with closed rectangular cross-section. *Acta Mechanica et Automatica* 2025; 19(2): 189-196. https://doi.org/10.2478/ama-2025-0022.
49. Suzuki H, Kinjo T, Hayashi Y, Takemoto M, Ono K. Wavelet Transform of Acoustic Emission Signals. *Journal of Acoustic Emission* 1996; 14(2): 69-84.
50. Samborski S, Rzeczkowski J, Korzec-Strzałka I. Experimental study of delamination process in elastically coupled laminates with the acoustic emission technique. *Engineering Structures* 2024; 300: 117196. https://doi.org/10.1016/j.engstruct.2023.117196.
51. Rzeczkowski J. Application of an unsupervised deep learning framework for acoustic emission-based characterization of delamination process in composite laminates. *Composites Science and Technology* 2026; 276: 111507. https://doi.org/10.1016/j.compscitech.2025.111507.
52. Liu Y, Huang K, Wang ZX, Li Z, Chen L, Shi Q, Yu S, Li Z, Zhang L, Guo L. Cross-scale data-based damage identification of CFRP laminates using acoustic emission and deep learning. *Engineering Fracture Mechanics* 2023; 294: 109724. https://doi.org/10.1016/j.engfracmech.2023.109724.
53. Hoseinlaghab S, Farahani M, Safarabadi M, Nikkhah M. Tension-after-impact analysis and damage mechanism evaluation in laminated composites using AE monitoring. *Mechanical Systems and Signal Processing* 2023; 186: 109844. https://doi.org/10.1016/j.ymssp.2022.109844.
54. Du J, Wang H, Cheng L, Bi Y, Yang D. Damage Localization, Identification and Evolution Studies during Quasi-Static Indentation of CFRP Composite Using Acoustic Emission. *Polymers* 2023; 15: 4633. https://doi.org/10.3390/polym15244633.
55. Arumugam V, Sajith S, Stanley AJ. Acoustic Emission Characterization of Failure Modes in GFRP Laminates Under Mode I Delamination. *Journal of Nondestructive Evaluation* 2011; 30: 213-219. https://doi.org/10.1007/s10921-011-0109-5.
56. Ghadarah N, Ayre D. A Review on Acoustic Emission Testing for Structural Health Monitoring of Polymer-Based Composites. *Sensors* 2023; 23: 6945. https://doi.org/10.3390/s23156945.
57. Lei Z, Pan R, Sun W, Dong Y, Wan Y, Yin B. Fatigue damage mechanisms and evolution of residual tensile strength in CFRP Composites: Stacking sequence effect. *Composite Structures* 2024; 330: 117818. https://doi.org/10.1016/j.compstruct.2023.117818.
58. Hong C, Lee S, Ji W. Shear strength determining mechanism of a +/ 45 laminate under tensile loading. *Composite Structures* 2023; 326: 117627. https://doi.org/10.1016/j.compstruct.2023.117627.
59. Zhong Z, Wang F, Kong F, Chen Y. Study of fatigue damage behavior in off-axis CFRP composites using digital image correlation technology. *Heliyon* 2024; 10: e25577. https://doi.org/10.1016/j.heliyon.2024.e25577.